Vanadium-Doped Hexagonal MoO_3: Structural and Electrochemical Characterization for Aluminium-Ion Battery Applications

Paloma Almodóvar [1, *], Joaquín Calbet [1,2], Inmaculada Álvarez-Serrano [2], Enrique Rodríguez-Castellón [3], Joaquín Chacón [1], María Luisa López [2], Carlos Díaz-Guerra [4].

[1] Zelestium Technologies, 42110 Soria, Spain.
[2] Departamento de Química Inorgánica, Facultad de Químicas, Universidad Complutense de Madrid, 28040 Madrid, Spain.
[3] Departamento de Química Inorgánica, Facultad de Ciencias, Universidad de Málaga, Campus de Teatinos, 29071, Málaga, Spain
[4] Departamento de Física de Materiales, Facultad de Físicas, Universidad Complutense de Madrid, 28040 Madrid, Spain.
* Corresponding author. Phone number: +34 627195941, e-mail: palmodov@ucm.es

Abstract

Vanadium-doped hexagonal molybdenum trioxide (h-MoO_3) has been systematically investigated as a cathode material for aluminium-ion batteries (AIBs). The evolution of the structural, morphological, compositional, optical, and electrochemical properties of h-MoO_3 doped with different vanadium concentrations were analysed by X-ray diffraction (XRD), micro-Raman spectroscopy, Fourier transform infrared spectroscopy (FTIR), scanning electron microscopy (SEM), high resolution transmission microscopy (HRTEM), SEM and TEM-energy-dispersive X-ray microanalysis (EDS), X-ray photoelectron spectroscopy (XPS), UV-Vis optical absorption and electrochemical techniques. Moderate vanadium doping maintains the hexagonal structure of the oxide host and does not adversely affect the crystallinity of the samples, while inducing morphological changes and local lattice distortions. Optical measurements revealed a significant reduction in the band gap by increasing the dopant concentration, suggesting enhanced electronic conductivity. Electrochemical studies demonstrated that vanadium incorporation improves charge transfer kinetics and cycling stability, with an optimal doping level corresponding to a V / Mo atomic ratio of 0.16, yielding a high specific capacity of ~240 $mA\,h\,g^{-1}$ at 100 $mA\,g^{-1}$ over 100 cycles. However, an excessive vanadium content led to secondary phase formation, structural degradation, non-homogeneous dopant spatial distribution, and decreased electrochemical performance. *Ex-situ* SEM-EDS and Raman analysis confirmed the excellent structural stability of vanadium-doped h-MoO_3 upon cycling, with uniform chloroaluminate species intercalation. These findings establish vanadium doping as an effective strategy to enhance h-MoO_3 for AIB applications, providing a balance between enhanced conductivity, electrochemical stability, and structural integrity.

Keywords: Aluminium-ion batteries, h-MoO_3, vanadium doping, cathode materials, energy storage.

1. Introduction

The increasing demand for sustainable and high-performance energy storage systems has driven intensive research into alternative battery technologies beyond conventional lithium-ion batteries. Among these emerging technologies, aluminium-ion batteries (AIBs) have garnered significant attention due to aluminium's high natural abundance, low cost, and theoretical high capacity [1,2]. Furthermore, aluminium anodes exhibit excellent safety properties, reducing the risk of dendrite formation and thermal runaway, which are common concerns in lithium-ion batteries [1].

Despite these advantages, AIBs still face critical challenges, particularly in the search for high-capacity electrode materials electrochemically compatible with the system [1,3]. Transition metal oxides (TMO) as the host of the Al ions show promising capacity and energy density. However, the insertion process remains challenging in terms of large-scale applications due to the high charge density around Al^{3+} and poor cycling stability resulting from the structural collapse of the host material after prolonged cycling. To address these issues, ion doping and the use of nano-sized materials are regarded as effective approaches to improve structural stability. On the other hand, these oxides are generally characterized by their low electrical conductivity, which explains why they are usually combined with carbon-based materials to improve the electrochemical properties [4,5]. The choice of electrode materials is crucial as well, because it directly influences the energy density, cycling stability, and overall performance of the battery [5–7]. Among TMOs, hexagonal molybdenum trioxide (h-MoO_3) is regarded as a very attractive material for energy storage applications. The h-MoO_3 structure is build-up of corner-sharing chains of MoO_6 octahedra along the crystallographic *c* axis. These chains are connected through adjacent oxygens giving rise to a hexagonal symmetry with wide one-dimensional tunnels, which allows ion intercalation and reduces the corresponding diffusion/migration barrier into the host. Inside such tunnels, the hexagonal MoO_6 framework accommodates NH_4^+ cations, which are considered essential to assure the structural stability of this metastable molybdenum trioxide phase [8].

Another fundamental aspect of AIB development is the electrolyte composition, which significantly affects the electrode's compatibility, ionic conductivity, and overall efficiency. The most commonly used electrolyte in AIBs is based on 1-ethyl-3-methylimidazolium chloride (EMIC) mixed with aluminium chloride ($AlCl_3$), forming an $AlCl_4^-/Al_2Cl_7^-$ ionic complex [9]. The electrochemical reactions in this system are as follows:

Cathode reaction: $AlCl_4^- + 3e^- \leftrightarrow Al + 4Cl^-$

Anode reaction: $2Al + 7Cl^- \leftrightarrow Al_2Cl_7^- + 6e^-$

While EMIC-based electrolytes provide high ionic conductivity, they suffer from high cost and corrosivity, which limits their widespread application. In recent years, urea-based electrolytes ($AlCl_3$: Urea) have demonstrated promising performance, offering a cost-effective and less corrosive alternative while maintaining electrochemical compatibility with aluminium-ion systems [10–12].

Recent studies have demonstrated that h-MoO_3 exhibits excellent electrochemical compatibility with $AlCl_3$: urea electrolytes, leading to promising capacity results. Following the above mentioned strategies, the development of carbon-based composites (e.g., carbon nanotubes [13]) or metal doping (e.g., nickel doping [14]) have been explored to further enhance its performance. Vanadium doping has emerged as an effective strategy to tailor the electronic and structural properties of transition metal oxides, optimizing their conductivity, redox activity, and structural stability. In various battery systems, the incorporation of vanadium has been reported to enhance electrochemical stability, mitigate capacity fading, and improve cycling performance by stabilizing the host structure and facilitating ion diffusion [15–17]. Moreover, recent works evidence that $Mo_{2+x}VO_{9+z}$ mixed oxides with different crystal structures and V/Mo atomic ratios in the (0.33 – 0.40) range show promising results for long-term cyclability in Zn-ion batteries [18] and good capacity for Al-ion batteries, but with a very reduced cyclability reported in the latter case (up to 30 cycles) [19].

Considering its favourable formation energy and structural compatibility with molybdenum, vanadium doping in h-MoO_3 is expected to enhance its electronic conductivity, redox activity, and overall electrochemical behaviour in AIBs [20]. Furthermore, Mo and V show several stable oxidation states, which may facilitate charge redistribution to maintain charge neutrality within the host structure during the charge/discharge cyclic process. However, to the best of our knowledge, vanadium-doped hexagonal molybdenum oxide has not yet been explored in the context of aluminium-ion batteries.

In this work, we present a comprehensive study on vanadium-doped hexagonal MoO_3 as a cathode material for aluminium-ion batteries. We investigate the effects of vanadium incorporation on the structural, morphological, electronic, and electrochemical properties of h-MoO_3 using various characterization techniques. Our findings provide new insights into the potential of vanadium doping to enhance the performance of MoO_3-based cathodes in aluminium-ion batteries.

Experimental

2.1 Synthesis of V-doped h-MoO_3

The h-MoO_3 material used in this study was synthesized through a scalable precipitation method, as previously described in reference [21]. In brief, a 2 M solution was prepared by dissolving 1.22 g of ammonium heptamolybdate tetrahydrate (AHM, $(NH_4)_6Mo_7O_{24}\bullet 4H_2O$, Sigma-Aldrich, 99.98%) in distilled water under magnetic stirring. Concentrated nitric acid (HNO_3 66%, Panreac) was then added dropwise to the solution, resulting in the formation of a white precipitate compound. The mixture was heated at 50 °C for 12 hours. Subsequently, the resulting powder was washed and filtered several times using distilled water and after dried in ambient air at 50 °C for 1 hour.

For the preparation of the doped materials, different concentrations of ammonium metavanadate (NH_4VO_3, Sigma Aldrich, >99%) were added to the initial solution. Throughout the entire precipitation process, constant magnetic stirring was maintained to ensure complete dissolution of the NH_4VO_3 and its homogeneous incorporation into the precursor mixture. The samples were labelled as follows based on the weight of NH_4VO_3 added relative to AHM: V0 (h-MoO_3, reference sample), V5 (0.05g), V10 (0.10 g), V15 (0.15 g), V20 (0.20 g), and V30 (0.30 g).

2.2 Characterization techniques

Long-range structural characterization of the samples was carried out by X-ray powder diffraction (XRD). XRD patterns were measured at room temperature with a PANanalytical X'PERT POWDER diffractometer using Cu Kα radiation ($\lambda = 1.5418$ Å). The diffraction profiles and the lattice parameters of the samples obtained have been performed using version 3 of the Match program. Short-range structural characterization was performed by micro-Raman spectroscopy and Fourier transform infrared spectroscopy (FTIR). Micro-Raman measurements were carried out at room temperature in a Horiba Jovin-Ybon LabRAM HR800 on an Olympus BX 41 confocal microscope system with a 633 nm He-Ne laser and an UV 325 nm He-Cd laser. Power density was carefully adjusted to maximize signal to noise ratio while avoiding irradiation-induced structural and compositional changes. Spectra shown in this work were recorded under the same experimental conditions for comparison purposes. FTIR spectra were recorded in the attenuated total reflection mode with a ThermoNicolet-6700 FT-IR spectrometer equipped with a MCT-A detector. The morphology of the samples was investigated with a FEI Inspect S scanning electron microscope (SEM). Their chemical composition and the corresponding elemental spatial distribution were assessed by energy dispersive X-ray spectroscopy (EDS, Bruker Quantax) in a Hitachi TM300 SEM equipped with a backscattered electron (BSE) detector. An accelerating voltage of 15 kV was used for EDS measurements. HRTEM images and selected area electron diffraction (SAED) patterns were obtained by using a JEOL JEM 3000 microscope operating at an accelerating voltage of 300 kV. Samples were prepared dispersing the powders in *n*-butanol and depositing drops of the solution onto porous carbon-coated copper grids. Semiquantitative chemical analyses and compositional mappings were carried out using EDS in STEM mode. UV-Vis/NIR optical absorption spectra were recorded in the (200-1800) nm spectral range by using a Jasco V770 spectrophotometer. X-ray photoelectron spectra (XPS) were performed in a Physical Electronics Versa Probe II Scanning XPS Microprobe spectrometer operating at base pressures $<10^{-6}$ Pa. The spectra were recorded at room temperature with a hemispherical energy analyzer with the equipment using a monochromatic Al Kα radiation source (1486.6 eV). The spectra were fitted by using the Gaussian–Lorentzian. As an internal reference for the binding energy, the adventitious carbon in C 1*s* region at 284.8 eV component was used.

2.3 Cell preparation and electrochemical techniques

The electrochemical tests were performed at room temperature in 13 mm diameter Swagelok-type cells (PTFE cell body and Mo plungers) assembled in an Ar-filled dry box, using graphite paper (Carbon-Foil, Goodfellow) with the same diameter as current collector (for both negative and positive electrodes). An Al metal foil (4N, 99.99%, Speira) of 12 mm diameter was employed as the negative electrode, while a Whatman GF/D borosilicate glass fibber sheet, saturated with a mixture of urea and $AlCl_3$ 1:1.3 by mol (IoLiTec), was used as electrolyte.

For the cathode, the h-MoO_3 active materials were mixed with carbon SP (Carbon black, Imerys) and sodium alginate (Sigma Aldrich) as conductive additive and binder, respectively, in deionized water, in a 70:20:10 ratio respectively. The obtained slurry was uniformly applied onto graphite paper using an automated Battery Slurry Electrode Film Coating Machine at a fixed height of 100 μm. Subsequently, the coated electrodes were dried overnight at 40 °C. Cathodes with a diameter of 13 mm and a targeted material loading of approximately 5 mg (~ 4 mg cm^{-2}) were prepared. The volume of electrolyte used corresponds to one-fourth of the deposited cathode material, measured in mL (*i.e.*, ~ 0.25 mL/mg).

Charge-discharge cycling, and cyclic voltammetry (CV) experiments were performed using an Arbin BT – 2143 Battery Tester potentiostat. The measurements were conducted in a voltage range of 0.4 V to 2.4 V to assess the electrochemical performance of the system (voltage limits where the response of the Urea-$AlCl_3$ electrolyte has been proved to be stable [14]). During charge-discharge experiments, the cells were subjected to a constant current of 100 mA g^{-1} to evaluate their energy storage capabilities. Cyclic voltammograms (CVs) were obtained by sweeping the voltage at different scan rates (1, 2, 5, 10, 20 mV s^{-1}), within the specified voltage range. This analysis aimed to study the redox behaviour of the system and identify any potential electrochemical reactions occurring during cycling. Electrochemical Impedance Spectroscopy (EIS) data were acquired using a Biologic BCS-815 battery tester by applying an AC voltage of 5 mV over a frequency range of 0.01 to 100 kHz. The acquired data were subsequently analysed using the BTS-Lab software. The EIS measurements were conducted under open-circuit voltage (OCV) after ten cycles with more than 30 mins of resting time.

2.4 Ex-situ electrode characterization

For the *ex-situ* characterization of the electrodes, the cells were disassembled in an Argon-filled dry box, and the electrodes were cleaned with *n*-butanol after discharge/charge to remove impurities. The *ex-situ* measurements were performed after completing 10 charge/discharge protocols ending in charge to facilitate the observation of the redox-active species inserted in the cathode.

3. Results and discussion

3.1 Morphological, structural, compositional and electronic characterization

The morphological evolution of the synthesized samples for increasing V concentration was analysed using SEM, and selected representative micrographs are presented in Figure 1. These images reveal significant changes in the rod-like morphology of hexagonal MoO_3 (h-MoO_3) upon vanadium doping. The V0 sample (Figure 1 (a)) exhibits well-defined prismatic hexagonal rods with lengths ranging between ~1 and 3 μm and diameters between ~300 nm and 1 μm. These observations are consistent with previous reports on h-MoO_3 synthesized via this precipitation method [8,21]. Upon vanadium incorporation, morphological modifications become evident. In sample V5 (Figure 1 (b)), the rods grow longer (~1 to 5 μm) and slightly thinner (200 to 500 nm in diameter), while maintaining their prismatic hexagonal shape in most cases. For the V10 sample (Figure 1 (c)), a further increase in vanadium content results in smoother rods with less-defined lateral facets. The rod dimensions remain comparable to those in V5, but larger rectangular agglomerates are occasionally observed. At higher doping levels (V15, Figure 1 (d))), a broader distribution of rod sizes emerges. The rod lengths range from 0.5 to 6 μm, while diameters vary between 200 nm and 1 μm. The prismatic hexagonal morphology is still present in a few rods, but larger particles become more frequent, suggesting increasing structural modifications. In the V20 sample (Figure 1 (e)), the rod size continues to decrease, with lengths ranging from 0.5 to 3 µm and diameters between 200 and 600 nm. The hexagonal morphology is observed in fewer rods, and most structures appear clustered together or as coatings over larger, smooth particles in the 5–50 µm size range.

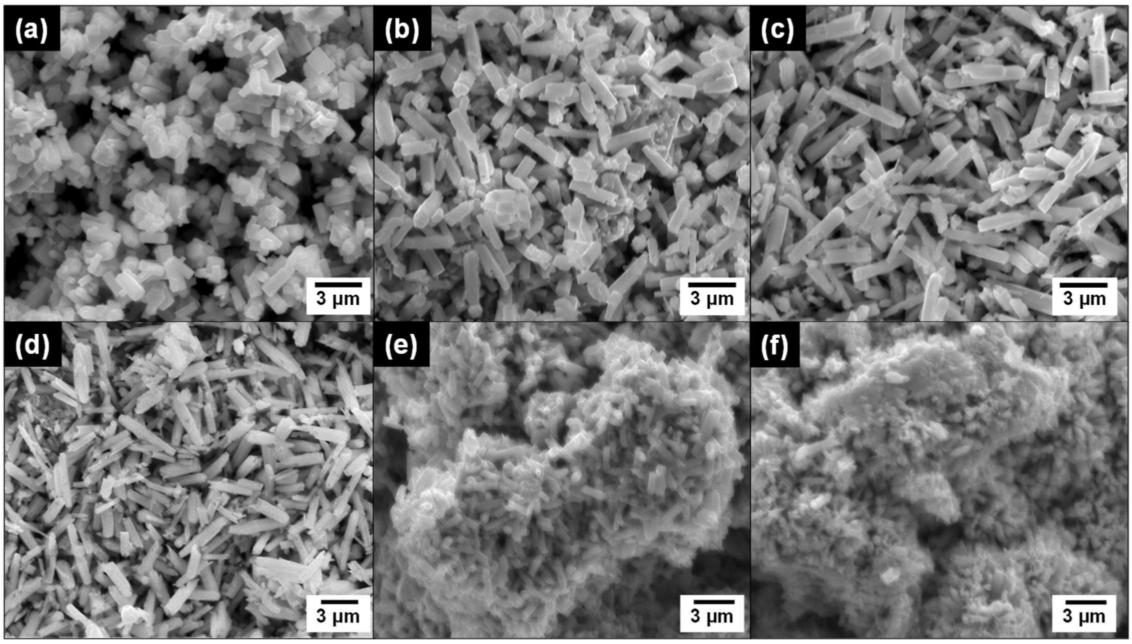

Figure 1. SEM micrographs of vanadium-doped hexagonal MoO_3 samples, showing morphological evolution with increasing vanadium content: (a) V0, (b) V5, (c) V10, (d) V15, (e) V20 and (f) V30.

Finally, the V30 sample (Figure 1 (f)) exhibits a highly irregular morphology. The rods become very small, appearing either in agglomerated clusters or dispersed over rough surfaces composed of submicrometric particles. The characteristic hexagonal rod-like shape is hardly recognizable, and at higher magnifications, the presence of filamentary nanostructures is occasionally observed. These results suggest that increasing vanadium content progressively disrupts the well-defined hexagonal rod morphology, leading to the formation of increasingly amorphous and aggregated structures.

To assess the composition of the samples, SEM-EDS measurements were carried out (Figure S1). The results confirm that the increase in vanadium content during synthesis correlates with a systematic rise in the V/Mo atomic ratio, as shown in Table I. The undoped reference sample (V0) contains no vanadium, while the doped samples exhibit progressively higher V/Mo ratios, ranging from 0.042 in V5 to 0.848 in V30. These results indicate a controlled incorporation of vanadium into the hexagonal MoO_3 structure, with higher precursor concentrations leading to greater vanadium substitution.

Table I. V / Mo atomic ratio determined by SEM-EDS analysis of the synthesized samples.

Sample	**V / Mo atomic ratio**
V0	0
V5	0.042
V10	0.088
V15	0.161
V20	0.342
V30	0.848

To investigate spatial distribution of the constituent elements, SEM-EDS elemental mappings were recorded from all samples. Figure 2 presents representative EDS mappings for the vanadium-doped materials (V5, V15, and V30), while a complete set of mappings for the remaining samples is provided in Figure S2.

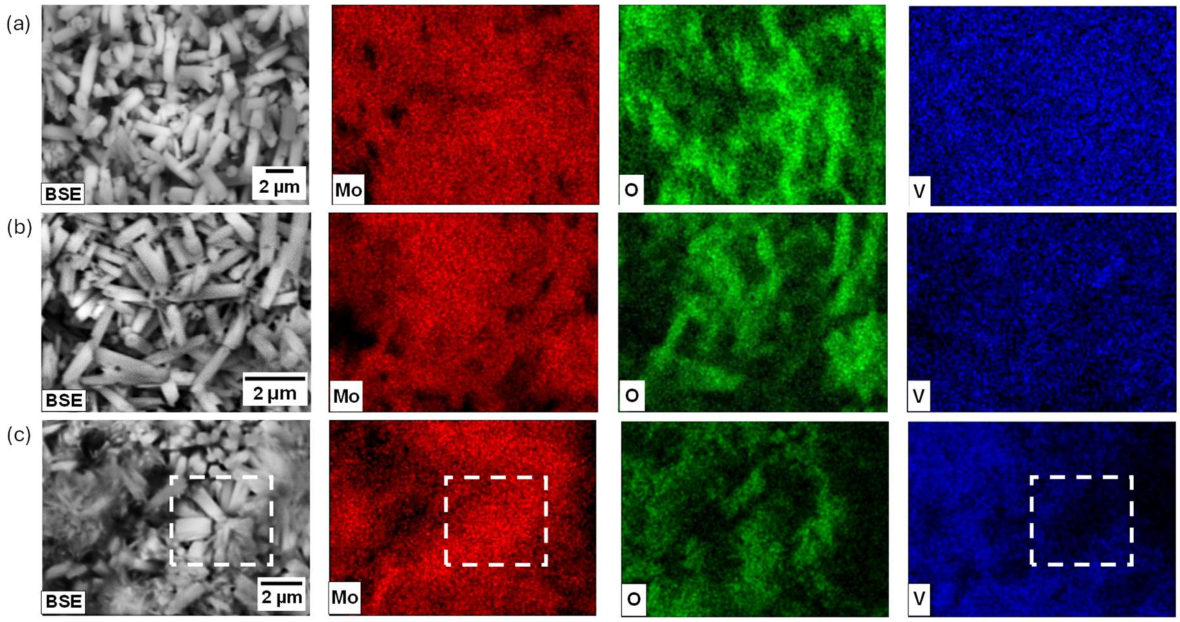

Figure 2. BSE images and corresponding Mo, O, and V EDS mappings of vanadium-doped h-MoO_3 samples: (a) V5, (b) V15, and (c) V30. It should be noted that EDS mappings of light elements, such as oxygen, may be affected by contrast artifacts arising from topography effects in non-flat samples.

In the V5, V10, and V15 samples, elemental maps reveal a homogeneous spatial distribution of vanadium, molybdenum, and oxygen, suggesting uniform incorporation of vanadium into the h-MoO_3 matrix. However, in the V20 and V30 samples, deviations from the typical hexagonal rod morphology become apparent. The presence of V- and Mo-rich regions suggests the formation of secondary phases or agglomerates, which may indicate phase segregation at higher doping levels. These results suggest that while low and moderate vanadium doping maintains the structural homogeneity, higher vanadium concentrations induce morphological and compositional inhomogeneities, potentially affecting the electrochemical behaviour of the material.

To complete the compositional analysis, X-ray Photoelectron Spectroscopy (XPS) measurements were conducted on the most representative samples (V0, V5, V10, and V15), selected for their homogeneous composition and to cover a range of vanadium doping concentrations. XPS survey spectra (Figure S3) confirm the presence of Mo, V, O, and C, while no additional elements were detected, in agreement with SEM-EDS results. Figures 3 (a) – (d) present the deconvolution of the high-resolution Mo 3*d* core-level spectra. The main contributions (97-99 %) centred at 236.3 eV and 233.1 eV correspond to the Mo $3d_3/_2$ and Mo $3d_5/_2$ binding energies of Mo^{6+}, with a spin–orbit splitting of $\Delta = 3.2$ eV. Additionally, weaker contributions (3-1%) appear at 235.5 eV and 232.4 eV, attributed to the Mo $3d_3/_2$ and Mo $3d_5/_2$ binding energies of Mo^{5+}, respectively.

These results are consistent with previous reports on MoO_3-based materials [14,22]. Interestingly, the Mo^{5+}/Mo^{6+} ratio is very low (< 0.04) and decreases with increasing V concentration, becoming negligible in sample V15, which strongly suggests that vanadium first fills the molybdenum vacancies. The high resolution V $2p_3/_2$ core level XPS spectra, Figures 3 (e) – (g), can be deconvoluted into two components: a dominant peak at 517.3 eV, corresponding to V^{5+}, and a weaker peak at 516.2 eV, associated with V^{4+} [23,24]. Regardless of the doping level, V^{5+} remains the predominant oxidation state, while the V^{4+}/V^{5+} ratio slightly decreases from 0.25 in V5 to 0.19 in V15. These findings suggest a progressive reduction in the concentration of oxygen vacancies in the pristine oxide upon vanadium doping. This behaviour contrasts with previous XPS studies on Ni-doped h-MoO_3, where the presence of nickel led to an increased oxygen vacancy concentration [14]. The high-resolution O 1s core-level spectra (Figure S4 (b)) can be deconvoluted into two main contributions at (530.9 ± 0.2) eV and (532.7 ± 0.1) eV. The lower binding energy peak is attributed to lattice oxygen bonded to Mo atoms, while the higher energy component is associated with Mo-OH or C-OH bonds. The binding energy positions of all deconvoluted peaks for Mo 3d and V 2p are summarized in Table II. Additionally, the V/Mo atomic ratios were measured by XPS (see Table S I) and found to be significantly higher than those obtained from SEM/EDS analysis. This suggests that vanadium is predominantly located at the surface of the samples.

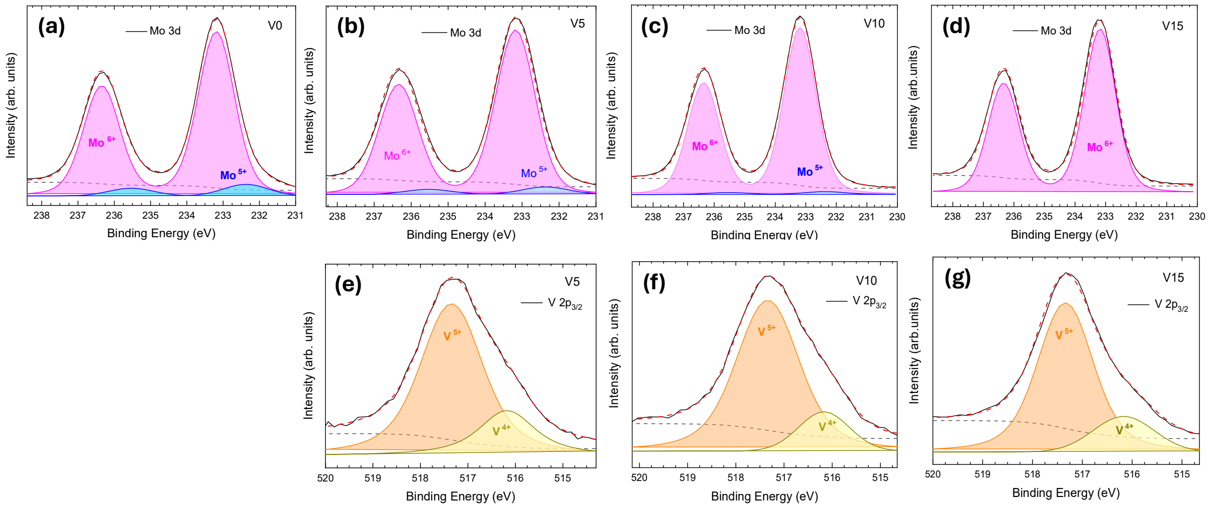

Figure 3. Mo 3d and V 2p core level XPS spectra of selected samples. (a–d) Mo 3d spectra for V0, V5, V10, and V15: Mo^{6+} (pink) and Mo^{5+} (blue) species. (e–g) V 2p$_{3/2}$ spectra for V5, V10, and V15: V^{5+} (orange) and V^{4+} (yellow) oxidation states.

Table II. Binding energy positions (eV) of Mo 3d and V 2p core-level peaks in selected samples, as determined from XPS analysis.

Sample	**Mo^{6+} 3d$_{3/2}$**	**Mo^{6+} 3d$_{5/2}$**	**Mo^{5+} 3d$_{3/2}$**	**Mo^{5+} 3d$_{5/2}$**	**V^{5+} 2p$_{3/2}$**	**V^{6+} 2p$_{3/2}$**
V0	236.3 eV	233.1 eV	235.5 eV	232.4 eV	-----	-----
V5	236.3 eV	233.1 eV	235.6 eV	232.4 eV	517.3 eV	516.2 eV
V10	236.3 eV	233.1 eV	235.6 eV	232.3 eV	517.3 eV	516.2 eV
V15	236.3 eV	233.1 eV	-----	-----	517.3 eV	516.2 eV

For clarity, a comparative plot of the Mo 3d, V 2p$_{3/2}$ and O1s deconvoluted spectra for all samples is provided in Figure S4 of the Supporting Information, allowing direct assessment of chemical state evolution with doping level.

To analyse the structural properties of the synthesized materials, XRD, micro-Raman spectroscopy, FTIR and TEM measurements were performed on the grown samples. The corresponding XRD patterns (Figure 4 (a)) could be indexed in all cases to the JCPDS file 01-

078-1027, corresponding to hexagonal MoO_3 (h-MoO_3). The lattice parameters and unit cell volume were calculated from the experimental data. While the *a* parameter does not show a well-defined trend upon increasing V content, the *c* axis parameter, as well as the unit cell volume, were found to decrease by increasing the V concentration (Figure 4(b)). In fact, the variation of the parameter *c* can be exclusively attributed to the incorporation of V to the host, since ammonium cations in the tunnels characteristic of the h-MoO_3 structure do not have any neighbours along the *c* axis. All samples exhibit high crystallinity, and vanadium incorporation appears to preserve the hexagonal structure, in agreement with previous reports [25]. However, subtle peak shifts, broadening effects, and enhanced diffraction maxima are observed in the doped samples. In particular, a progressive shift of the (008) diffraction maximum towards higher angles is observed as the vanadium content increases (Figure 4(c)).

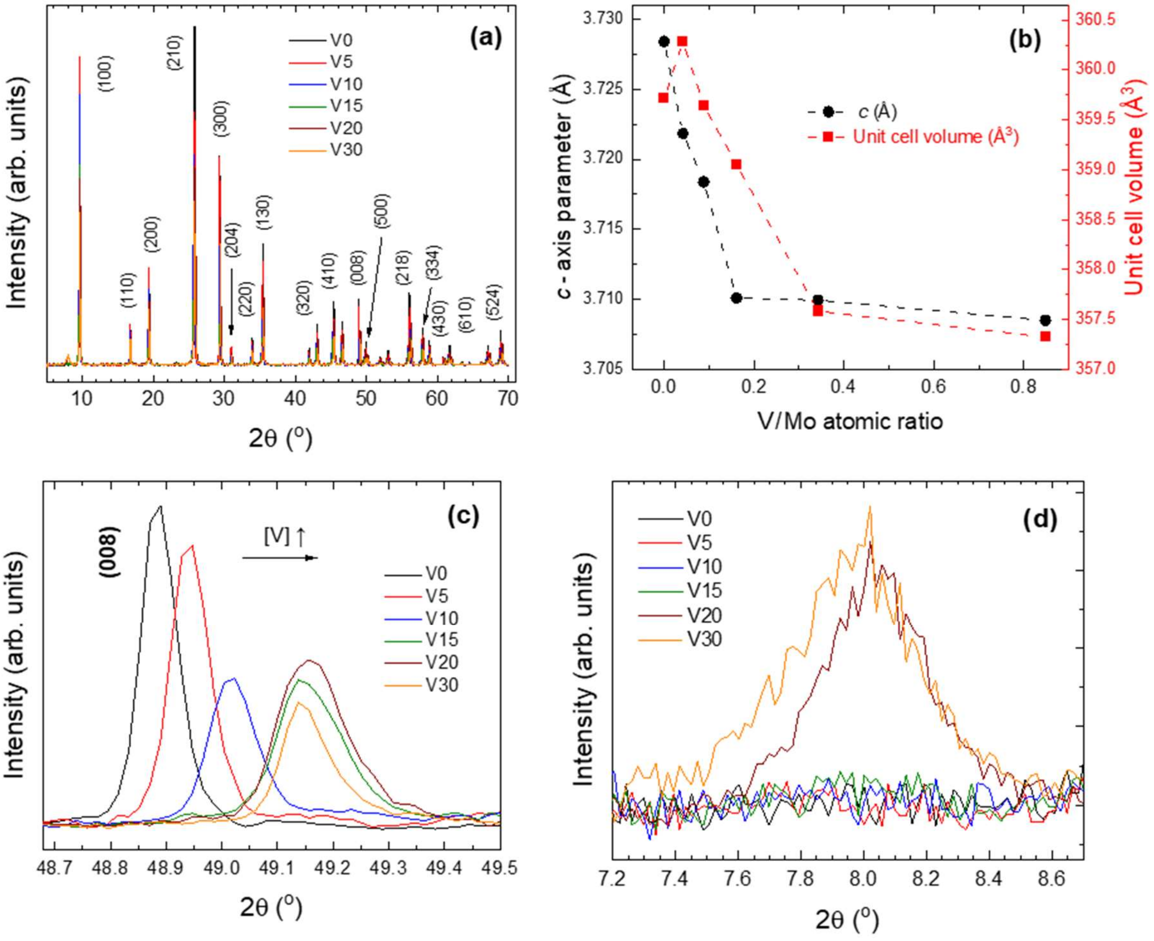

Figure 4. XRD patterns of vanadium-doped h-MoO_3 samples. (a) Full XRD patterns indexed to JCPDS file 01-078-1027. (b) c-axis parameter length and unit cell volume as a function of V content. (c) Progressive shift of the (008) diffraction maximum towards higher angles with increasing vanadium content. (d) Appearance of a new diffraction maximum at ~8.02° in diffraction patterns of samples doped with the higher V contents.

This shift is directly related to a reduction in the *c* lattice parameter. Since V^{5+} has a smaller ionic radius than Mo^{6+}, its incorporation into the h-MoO_3 structure leads to a contraction of the octahedral units, particularly along the *c*-axis. This structural contraction is consistent with the observed peak shift and provides further evidence that vanadium is successfully incorporated into the hexagonal molybdenum oxide framework, rather than forming separate phases at low or moderate doping levels. In addition, a new diffraction maximum at 8.02° (Figure 4 (d)) emerges for higher vanadium concentrations (samples V20 and V30), suggesting the formation of vanadium hydroxides or VO_x monomers, as further supported by Raman spectroscopy (see below). Similar diffraction features have been reported for $V_2O_5 \bullet nH_2O$ xerogels [26], reinforcing the hypothesis of secondary phase formation at elevated vanadium doping levels.

To further investigate the structural properties of the synthesized materials, micro-Raman spectroscopy was performed on all samples. Representative Raman spectra, presented in Figure 5(a), exhibit distinct vibrational bands at 133, 175, 220, 250, 312, 396, 413, 493, 689, 886, 901, 914, and 974 cm^{-1}, which are characteristic of h-MoO_3 [21,27]. The peaks located in the 885–975 cm^{-1} range can be assigned to symmetric and antisymmetric Mo=O stretching vibrations, while the 690 cm^{-1} band corresponds to O–Mo–O scissoring vibrations along the *c*-axis. Vibrational modes within the 495–315 cm^{-1} range are attributed to rocking and scissoring motions of O-Mo-O bonds in the *ab* planes, whereas bands between 315 and 220 cm^{-1} correspond to O-Mo-O twisting vibrations. Peaks observed below 180 cm^{-1} are associated with lattice modes [8]. Since vanadium is lighter than molybdenum, and both V^{5+} (0.59 Å) and V^{4+} have smaller ionic radii (0.54 Å and 0.58 Å, respectively) than Mo^{6+} (0.59 Å), their incorporation into the h-MoO_3 framework is expected to induce peak shifts towards higher wavenumbers. This effect is particularly evident in the 135 and 690 cm^{-1} bands, supporting the hypothesis that vanadium is successfully replacing molybdenum within the structure. Specifically, the 690 cm^{-1} peak, which corresponds to O-Mo-O scissoring along the *c*-axis, exhibits a clear shift towards higher wavenumbers (Figure 5(b)), consistent with the observed decrease in the *c* lattice parameter in the XRD analysis. In addition, broadening effects are observed in vibrational bands where atomic motion involves a significant contribution from the substituted Mo atoms. It is worth mentioning that a new Raman band, centred between 1014 and 1019 cm^{-1} (Figure 5 (c)), appears in the spectra of samples with higher vanadium content (V20 and V30). The intensity of this peak increases with vanadium concentration, suggesting the formation of V=O stretching vibrations of monomeric VO_x surface species, as previously reported in Raman studies of supported vanadium oxide catalysts [28,29].

FTIR spectra of all samples are shown in Figure 6(a). As in Raman spectra, broadening of the Mo–O vibration modes (Figure 6 (b)) is observed with higher vanadium incorporation, indicating increased structural disorder within the h-MoO_3 framework. These measurements confirm the presence of NH_4^+ groups, with peaks associated to different N-H bonds vibrations centred at about 1440, 1408 and 3220 cm^{-1} as well as OH^- groups (peaks at 1612 and 1650 cm^{-1}), which are known to play a key role in stabilizing the h-MoO_3 phase [8].

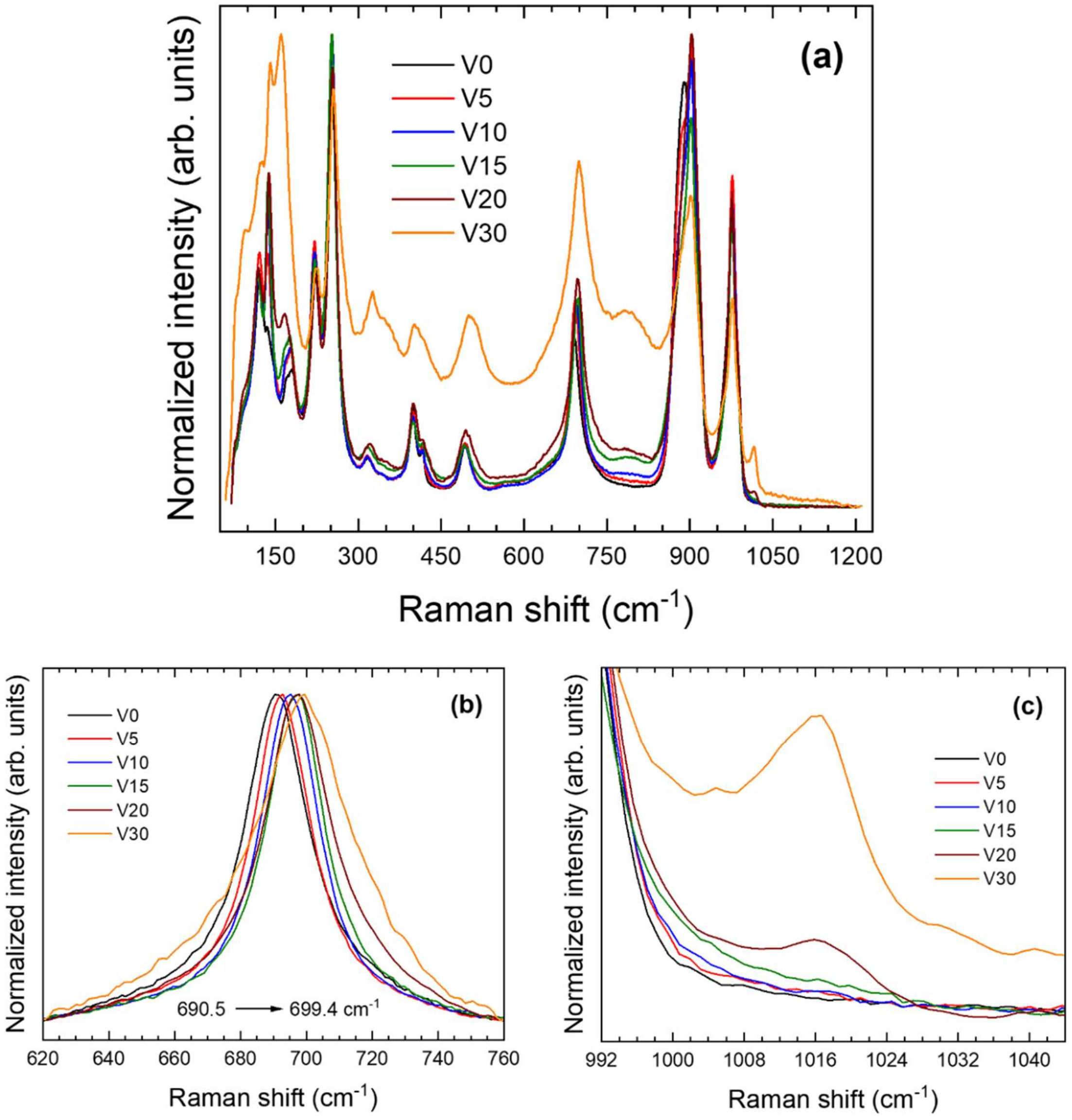

Figure 5. (a) Raman spectra of vanadium-doped h-MoO_3 samples showing peak shifts and intensity variations with increasing vanadium content. (b) Shift of the 690 cm^{-1} Raman peak upon doping (c) Magnified view of the (990–1045) cm^{-1} spectral range.

These characteristic vibrational modes are observed across all compositions, indicating that the fundamental structure remains intact upon vanadium doping. However, increasing vanadium content leads to a progressive decrease in the intensity of ammonium and hydroxyl-related bands, suggesting that these molecular species are gradually removed from the h-MoO_3 tunnel structure (Figures 6 (c), (d)). Such structural modification could potentially enhance the insertion and extraction of chloroaluminate ions, which is crucial for electrochemical applications. These FTIR results further support the occurrence of structural changes induced by vanadium doping, in agreement with XRD and Raman findings.

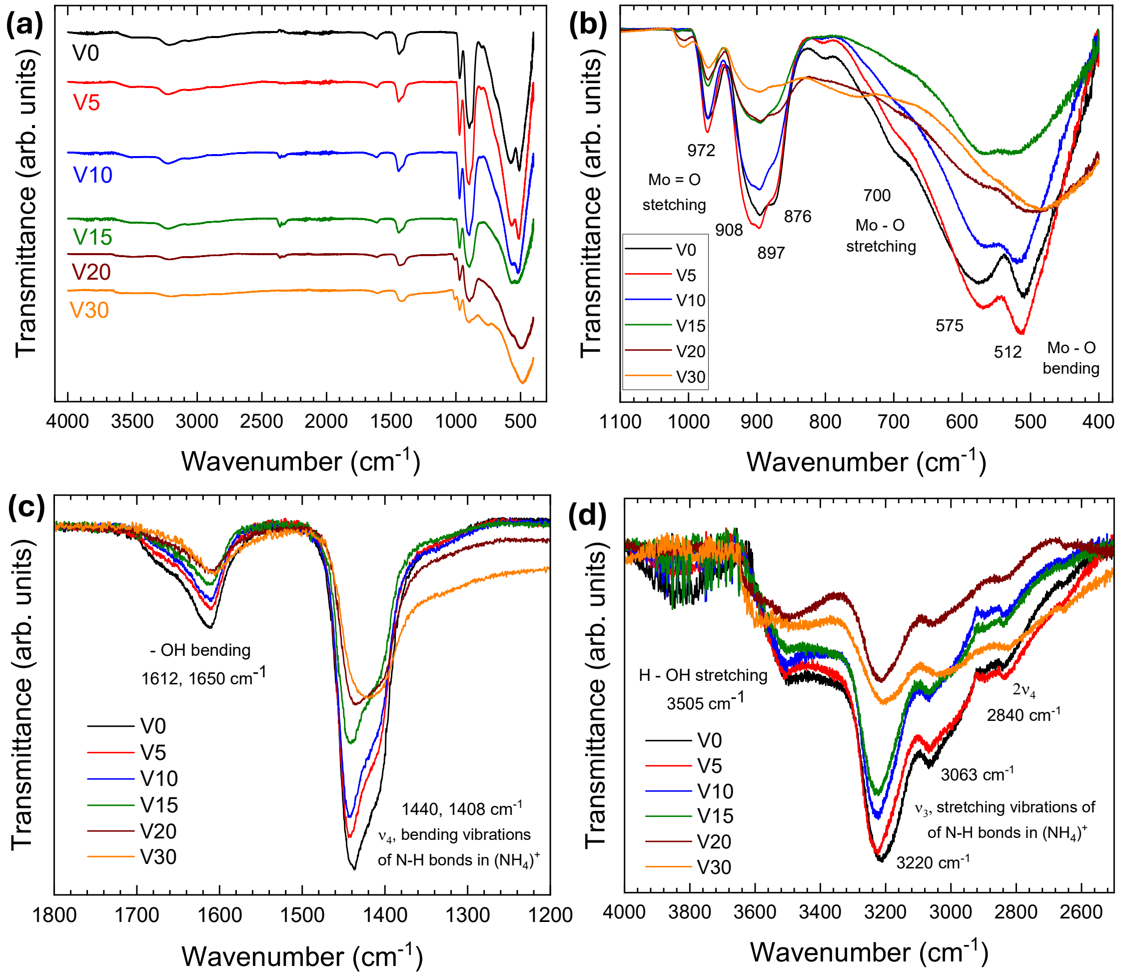

Figure 6. (a) FTIR spectra of vanadium-doped h-MoO_3 samples. (b) Mo=O and Mo–O stretching and bending IR modes. Evolution of bands associated to bending (c) and stretching vibrations (d) involving NH_4^+ and OH^- groups upon increasing vanadium concentration.

In order to get further insight into the structural properties of our materials, HRTEM and SAED analyses were performed on undoped and vanadium-doped h-MoO_3 samples to assess their crystallinity and the distribution of vanadium within the microstructures (Figures 7 and S5). For the undoped sample (V0), HRTEM images and SAED patterns confirmed the expected hexagonal h-MoO_3 phase, showing well-crystallized rods with clear lattice fringes (Figure S5 (a,b)). However, these structures exhibited high sensitivity to electron beam exposure, leading to rapid amorphization under prolonged irradiation. For moderately doped samples (up to V15), HRTEM and SAED analysis confirmed that the hexagonal phase was maintained, with no severe apparent structural distortions induced by vanadium incorporation.

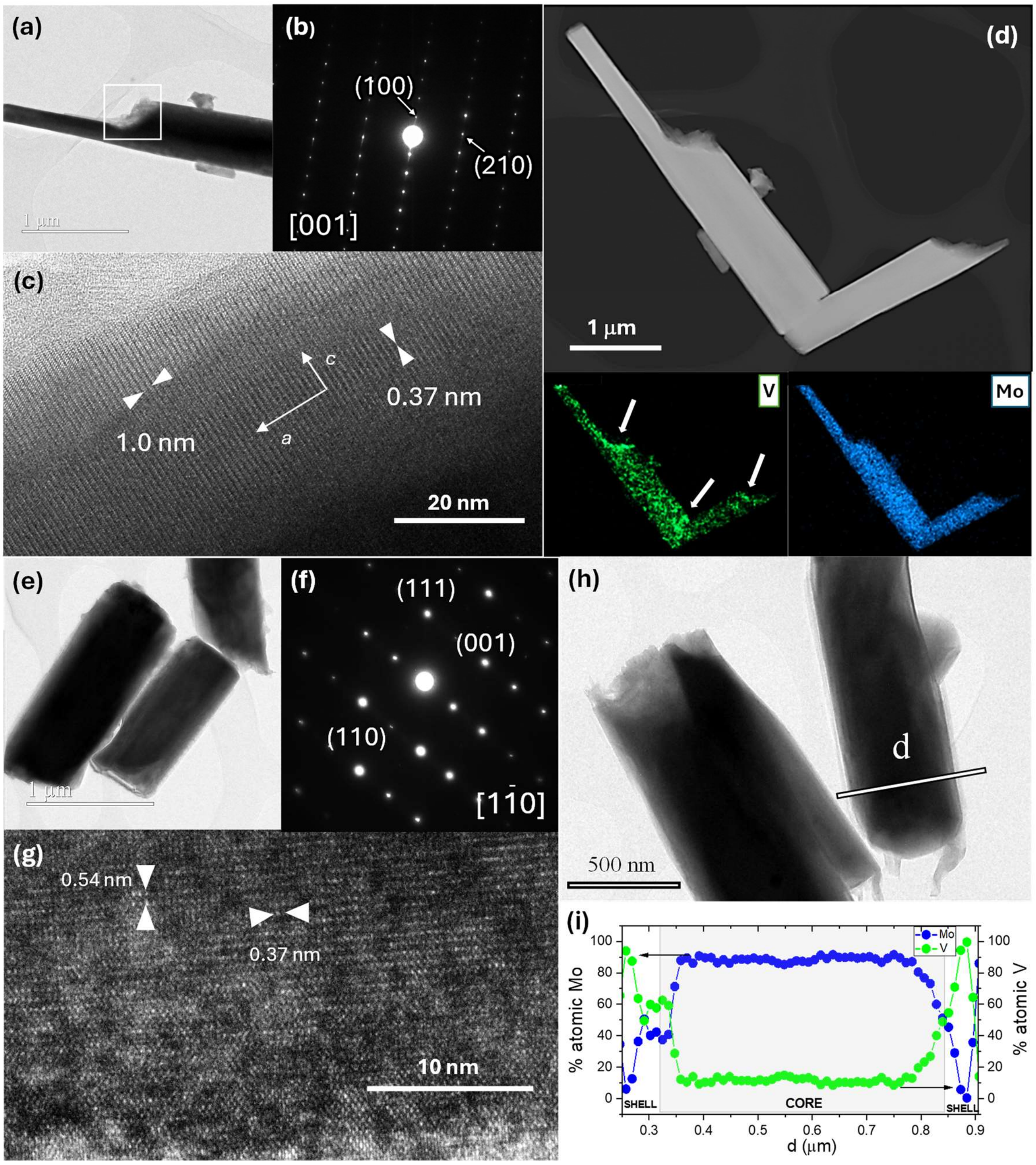

Figure 7. TEM characterization of vanadium-doped h-MoO$_3$ samples. V15 sample: (a) Low-magnification TEM image, (b) SAED pattern along the [001] zone axis, (c) HRTEM and (d) know magnification image showing a couple of rods and corresponding STEM-EDS Mo and V elemental mappings. White arrows mark V-rich tips of the rods. V20 sample: (e) TEM image, (f) SAED pattern along the [110] zone axis, (g) HRTEM micrograph and (h) - (i) Low

magnification image showing some rods and STEM-EDS line scan across the marked micro-rod evidencing Mo and V distribution conforming a core-shell structure.

Figures 7(a–c) present the analysis corresponding to the V15 sample, chosen as a representative case for samples with moderate vanadium content (V5 - V15), which exhibited analogous structural features. The high-resolution micrographs displayed well-defined lattice fringes, while the corresponding SAED patterns were consistent with highly crystalline h-MoO_3. EDS elemental mappings (Figure 7(d)) confirmed a rather homogeneous distribution of vanadium within the micro-rods, reinforcing the conclusion that it is successfully incorporated into the MoO_3 lattice. Nevertheless, the progressive addition of vanadium was found to lead to an increased concentration of this element at the tips of the rods first and then over the whole surface of the microstructures (see Figure 4(d) and S5 (d,e)), in agreement with the XPS results, which indicate a higher V/Mo atomic ratio on the surface compared to bulk measurements. Actually, for higher doping concentrations (V20 and V30), the HRTEM images and SAED patterns resembled those of the undoped sample but exhibited increased structural degradation under the electron beam, suggesting reduced crystallinity. Notably, the presence of layered and filamentary structures showing a lighter contrast and located at the ends of the micro-rods or coating them was clearly observed, as shown in Figures 7(e,h), which correspond to the V20 sample. These structures indicate the emergence of a secondary vanadium-rich phase, forming an external layer around the rods, as shown in the previously mentioned EDS mappings. To confirm this fact, several compositional line profiles across the microstructures were recorded. An example is shown in Figures 7(h–i)), confirming that vanadium segregates towards the rod surfaces, forming a distinct core-shell structure in V20 and V30. In these samples, a vanadium-rich shell (~0.1 μm thick) surrounds a vanadium doped h-MoO_3 core, in agreement with the XRD and Raman results, where the appearance of secondary vanadium-based phases was also detected. This phase is likely a vanadium hydroxide or oxyhydroxide, as suggested by previous spectroscopic analyses. These results confirm that at moderate doping levels (V5–V15), vanadium is effectively incorporated within the MoO_3 framework, whereas higher doping concentrations (V20 and V30) lead to phase segregation, forming an external vanadium-rich shell around the micro-rods. Moreover, it is worth mentioning that the local V/Mo atomic ratios obtained by TEM-EDS on individual microrods were consistent with the nominal doping levels and with the values derived from SEM-EDS analysis, further confirming the successful incorporation of vanadium during synthesis.

The optical properties of the vanadium-doped h-MoO_3 samples were investigated through diffuse reflectance spectroscopy. The normalized reflectance spectra, presented in Figure 8(a), reveal a significant shift in the absorption edge with increasing vanadium content, indicating a reduction in the optical band gap (E_g). The estimated indirect optical band gap values, calculated from Tauc plots using the Kubelka-Munk function (Figure S6), are summarized in Figure 8(b). Upon vanadium incorporation, the optical band gap undergoes a substantial reduction, particularly at low doping levels. The transition from pure h-MoO_3 ($E_g = 2.87$ eV) to vanadium-doped samples results in a sharp initial decrease, followed by a more gradual shrinkage as the V/Mo ratio increases. The lowest band gap value (1.83 eV) is observed for V30, suggesting that vanadium incorporation effectively modifies the electronic structure of the material. According to the XPS analysis, although a partial reduction of Mo^{6+} to Mo^{5+} is observed upon vanadium doping, the overall Mo^{5+}/Mo^{6+} ratio remains low across all samples. In addition, no characteristic absorption bands associated with oxygen vacancies were detected in the UV-Vis spectra, suggesting that such defects are not a dominant factor influencing the electronic behaviour in the present system.

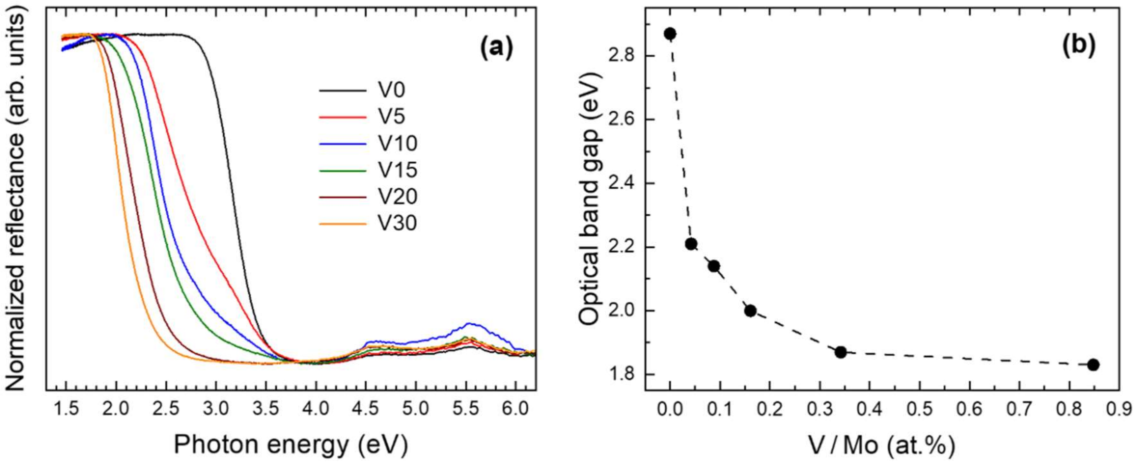

Figure 8. Optical characterization of vanadium-doped h-MoO_3 samples. (a) Normalized reflectance spectra. (b) Variation of the estimated indirect optical band gap (E_g) as a function of the V/Mo atomic ratio.

These results confirm that vanadium doping plays a crucial role in tuning the electronic and optical properties of h-MoO_3, which could be advantageous for energy storage applications where an optimized electronic conductivity is required. In addition, V incorporation was found to modify the absorbance spectra of the sample, introducing bands in the visible range that can be assigned to charge transfer transitions involving V^{5+} and V^{4+} ions (Figure S7).

3.2 Electrochemical characterization

Before starting the electrochemical characterization of the synthesized samples, electrochemical measurements were performed on both the graphite paper current collector and the carbon black used in the slurry preparation to verify that it did not significantly contribute to the observed capacity values. The results of this study have been previously reported in an earlier work and reveal a negligible contribution of both elements to the measured capacities [14].

To evaluate the electrochemical performance of the vanadium-doped h-MoO_3 samples, cyclic voltammetry (CV), electrochemical impedance spectroscopy (EIS), and galvanostatic charge-discharge (GCD) measurements were conducted. Cyclic voltammograms of all samples at 1 mV s^{-1}, normalized to current density per gram of active material, are presented in Figure 9(a). The CV profiles of V0, V5, V10, and V15 exhibit similar shapes, with a progressive increase in the enclosed area as the vanadium content increases. This behaviour suggests a gradual enhancement in electrochemical activity, potentially associated with improved charge transfer and ion diffusion kinetics. However, for the V20 and V30 samples, the enclosed area in the CVs decreases, which may be attributed to the presence of secondary phases, as previously observed in the structural characterization. The Nyquist plots of all samples are displayed in Figure 9(b). While all vanadium-doped samples exhibit similar impedance profiles, a notable increase in the slope of the low-frequency region is observed with increasing vanadium content up to V15. This trend suggests an improvement in charge transfer and electrochemical kinetics due to vanadium incorporation. However, for V20 and V30, the slope begins to decrease again, consistent with the CV results, indicating that excessive vanadium doping may hinder electrochemical performance.

The discharge capacities of all samples, cycled at a current density of 100 mA g^{-1}, are shown in Figure 9(c). The initial capacity decay observed in samples V0–V20 is typical of electrode activation processes, including interface stabilization and reorganization of ion diffusion pathways. Interestingly, the V30 sample shows an initial increase in capacity during early cycles, which may be attributed to delayed electrochemical activation due to its core–shell morphology and partial phase segregation, as evidenced by TEM and EDS analyses. The results demonstrate a progressive increase in the stabilized discharge capacity with increasing vanadium content, reaching a maximum of ~240 mA h g^{-1} for V15. While V20 initially exhibits similar or slightly higher capacities than V15, it undergoes rapid degradation after ~20 cycles, suggesting structural instability. In contrast, the V30 sample displays lower discharge capacities than the undoped material (V0), indicating that excessive vanadium incorporation negatively impacts electrochemical performance. These findings highlight the existence of an optimal vanadium doping concentration, beyond which the electrochemical activity deteriorates. It is worth mentioning that the coulombic efficiency of the samples, remains above 95% once the capacity stabilizes in all samples (Figure S8).

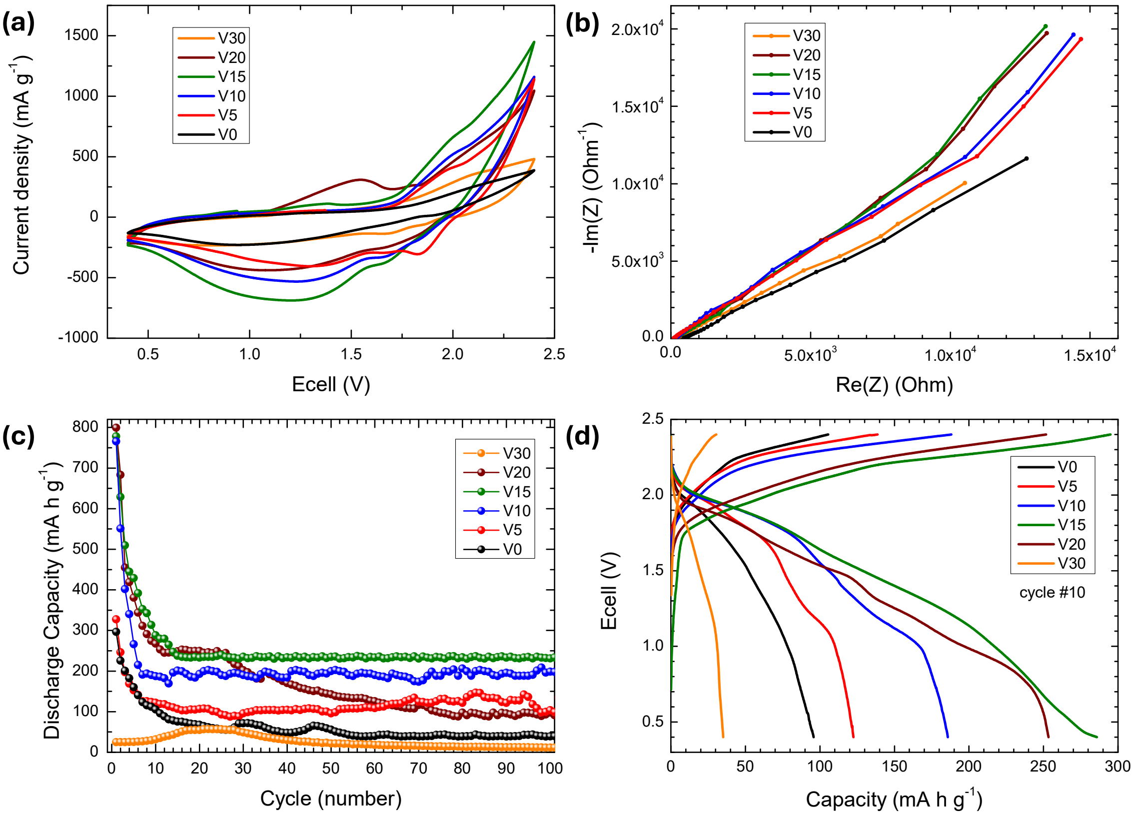

Figure 9. Electrochemical characterization of vanadium-doped h-MoO_3 samples. (a) Cyclic voltammograms (CV). (b) Nyquist plots obtained from EIS. (c) Discharge capacity as a function of cycle number at 100 mA g^{-1}. (d) Galvanostatic discharge profiles at cycle 10.

Additionally, we emphasize that the 100-cycle galvanostatic tests conducted for each sample required continuous operation over periods ranging from approximately one to three months, depending on the specific capacity and cycling stability. Notably, the V15 sample, which exhibited the highest specific capacity, also required the longest measurement time. Thus, the 100-cycle duration offers a robust and consistent evaluation of the long-term electrochemical behaviour, allowing for meaningful comparison across the different compositions studied.

To conduct a more detailed assessment of the electrochemical properties, discharge profiles at cycle 10 (before V20 degradation begins) are compared in Figure 9(d). Vanadium incorporation introduces a new discharge plateau at ~1.2 V, whose contribution increases progressively with doping concentration up to V15. However, in V20, the plateau exhibits a distinct behaviour, with lower voltages than in the other samples, suggesting that beyond this doping level, the electrochemical interaction is significantly altered.

These electrochemical results confirm that vanadium doping enhances the performance of h-MoO_3 electrodes, improving charge transfer efficiency and cycling stability. However, excessive vanadium incorporation leads to structural and electrochemical instabilities, ultimately degrading battery performance. The improved electrochemical performance observed upon moderate vanadium doping can be directly correlated to the structural modifications induced in the h-MoO_3 lattice. The reduction in the *c*-axis lattice parameter (as evidenced by XRD) and the shifts in the O–Mo–O vibrational modes (observed by Raman spectroscopy) suggest a tighter and more rigid framework that facilitates the diffusion of chloroaluminate species through the one-dimensional tunnels. Moreover, the significant decrease in the optical band gap revealed by UV-Vis absorption measurements indicate an enhanced electronic conductivity, which contributes to improve the efficiency of charge transfer processes during battery operation. Notably, the doping limit appears to be directly related to the formation of secondary phases, as previously observed in the structural characterization. At moderate doping levels, vanadium integrates well into the h-MoO_3 framework, preserving the hexagonal structure and contributing to enhanced electrochemical behaviour. However, beyond a critical doping concentration (V (at.%) / Mo (at.%) > 0.161), the emergence of V-rich secondary phases disrupts the electrode's structural integrity, altering ion diffusion pathways and reducing electrochemical reversibility. This structural destabilization correlates with the observed capacity fading and changes in the discharge profile, indicating that excessive vanadium incorporation hinders, rather than enhances, the electrode's performance. A comparison with previous studies on Ni-doped h-MoO_3 further highlights the advantages of vanadium incorporation [14]. While both doping strategies yield similar stabilized discharge capacities (~ 240 mA h g^{-1}), vanadium-doped samples require significantly lower amounts of carbon black and binder (70:20:10 vs. 55:25:20 in the Ni-doped system). This suggests that vanadium enhances the intrinsic electronic conductivity and structural integrity of h-MoO_3, minimizing the need for additional conductive additives and improving electrode efficiency. Moreover, vanadium doping leads to a more stable charge-discharge response, with less fluctuation in capacity retention compared to Ni-doped h-MoO_3. This improved cycling stability indicates that vanadium incorporation reinforces the electrode structure, reducing material degradation over prolonged use. Overall, these findings demonstrate that vanadium doping is a more effective strategy for optimizing the electrochemical performance of h-MoO$_3$. It enables higher capacity retention, greater cycling stability, and a reduced reliance on inactive electrode components, making it a more practical and cost-effective approach for next-generation aluminium-ion batteries.

To further explore the insertion mechanisms occurring at the main redox peaks and evaluate the impact of vanadium incorporation, cyclic voltammetry (CV) measurements at different scan rates were performed on V0, V10, and V15 (Figure 10 (a–c)). With increasing scan rates, the redox peaks located at ~ 1.95 V (intercalation) and ~1.2 V (deintercalation) exhibited an increase in current density and a shift toward higher and lower voltages, respectively, as expected for diffusion-dependent processes. This behaviour follows the relationship described by the power law equation $i = av^b$, where i represents the measured current, v is the scan rate, and a and b are adjustable parameters. The b parameter, obtained from the slope of the log(i) vs. log(v) plot, provides insight into the dominant charge storage mechanism: $b \approx 0.5$ suggests a diffusion-controlled process, indicating that ion insertion/extraction kinetics are limited by solid-state diffusion within the electrode. Meanwhile, $b \approx 1.0$ corresponds to a (pseudo)capacitive behaviour, where charge storage is primarily surface controlled [30].

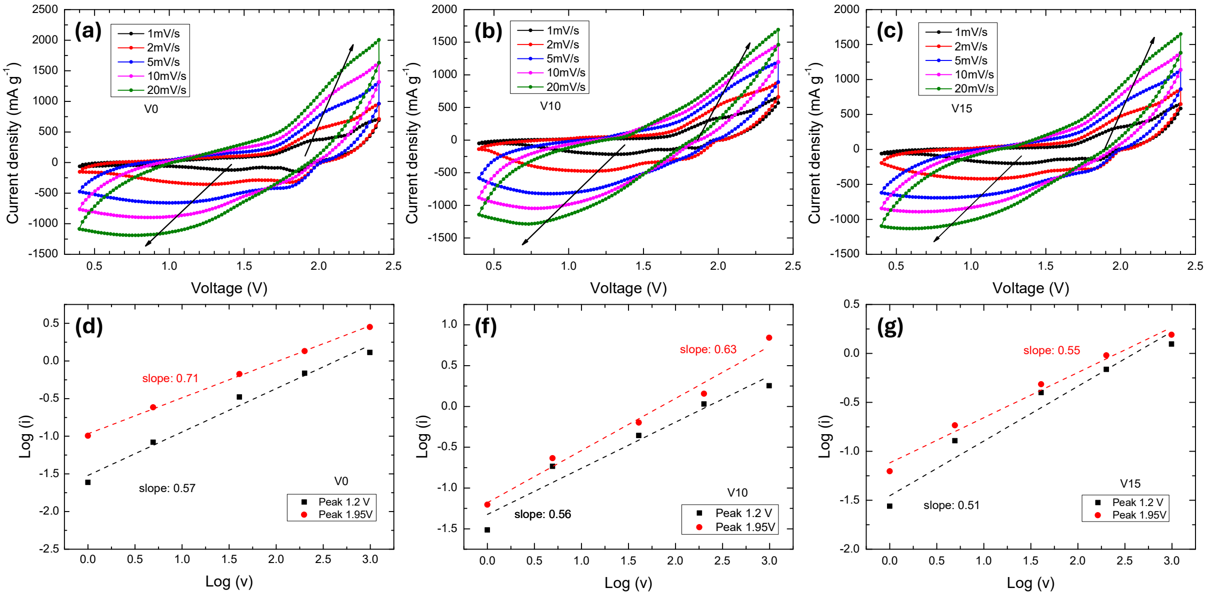

Figure 10. Cyclic voltammetry (CV) analysis at different scan rates for selected vanadium-doped h-MoO$_3$ samples. (a–c) CV curves of V0, V10, and V15, showing the evolution of redox peaks at increasing scan rates. (d–g) Log(i) vs. log(v) plots for the main redox peaks (~1.2 V and ~ 1.95 V).

As shown in Figures 10 (d–g), regression analysis revealed a progressive decrease in the *b* value with increasing vanadium content, with V15 exhibiting values closer to 0.5 for both intercalation (~ 1.95 V) and deintercalation (~1.2 V) peaks. This suggests that vanadium incorporation enhances diffusion-controlled charge storage, favouring a pronounced battery-like behaviour.

This trend is particularly relevant in the context of electrode design for aluminium-ion batteries. Similar diffusion-controlled mechanisms have been observed in transition metal oxides for lithium-ion and sodium-ion batteries, where improved ion intercalation kinetics lead to enhanced capacity retention and prolonged cycling stability [31]. These findings reinforce that vanadium doping not only enhances the electrochemical capacity but also shifts the charge storage mechanism toward more efficient intercalation kinetics.

To further investigate the structural stability of the best-performing electrode, ex situ SEM-EDS mapping and Raman spectroscopy were performed on the V15 sample after cycling. Figure 11(a–e) presents the SEM-EDS elemental mapping. The hexagonal morphology of the material is well preserved after cycling, indicating that the structural integrity of h-MoO_3 remains intact during electrochemical operation. The elemental distribution maps reveal a homogeneous dispersion of aluminium throughout the electrode, confirming that the redox processes occur uniformly within the material. This observation suggests that chloroaluminate redox-active species undergo effective intercalation and deintercalation within the material, without inducing significant phase segregation or structural degradation.

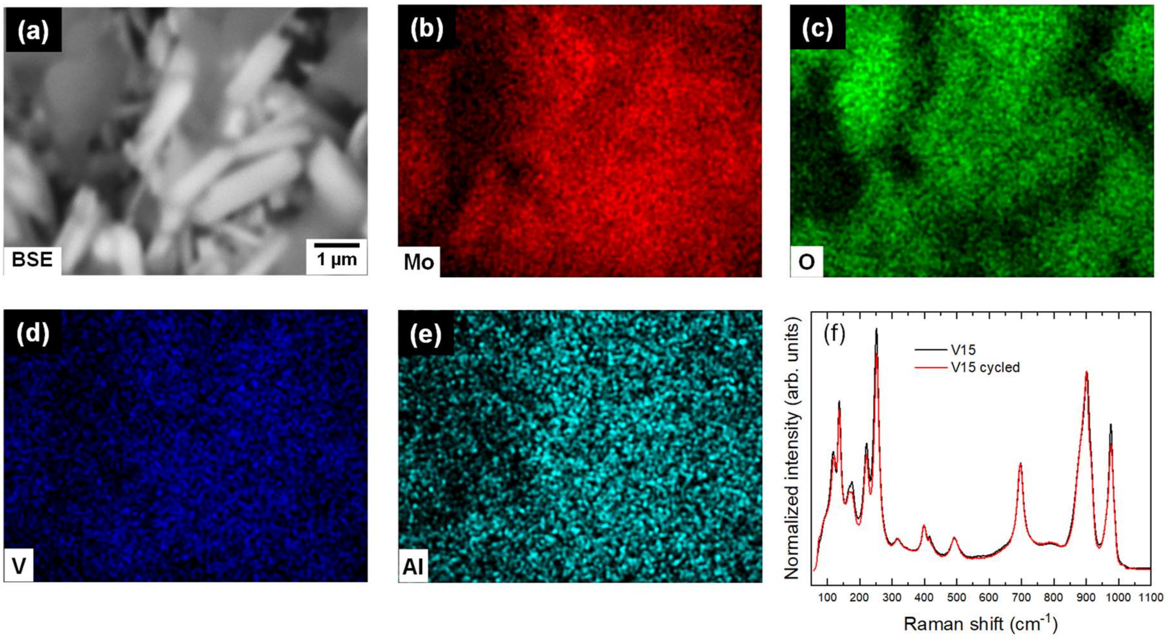

Figure 11. Ex situ characterization of the V15 electrode after cycling. (a) BSE-SEM image. (b–

e) EDS elemental mapping of Mo, O, V, and Al. (f) Comparative Raman spectra of h-MoO_3 before and after cycling.

Additionally, comparison of Raman spectra the Raman spectra of the V15 electrode before and after cycling are shown in Figure 11(f). The results demonstrate that the original structure is maintained, with no new phases detected after electrochemical cycling. This finding highlights the high structural stability of vanadium-doped h-MoO_3 as an electrode material in aluminium-ion batteries, reinforcing its potential for long-term electrochemical applications. Our results confirm that V15 maintains its crystallographic integrity and electrochemical activity over prolonged cycling, making it a promising candidate for high-performance aluminium-ion batteries.

4. Conclusions

Vanadium doping is an effective strategy to significantly improve the electrochemical performance of hexagonal molybdenum trioxide (h-MoO_3) as a cathode material for aluminium-ion batteries (AIBs). Moderate vanadium doping induces morphological changes and local lattice distortions but maintains the hexagonal structure of the oxide host and does not adversely affect the crystallinity of the samples, which correlates with an improvement in the electrochemical behaviour. However, at higher doping levels, the formation of secondary phases was observed, leading to structural instability and diminished electrochemical performance. The impact of vanadium doping on the electronic properties of h-MoO_3 is revealed by optical absorption measurements, evidencing a noticeable band gap reduction, which decreased from 2.87 eV (undoped h-MoO_3) to ~1.85 eV (samples with the higher V contents). This band gap shrinkage suggests an enhancement in electronic conductivity, facilitating more efficient charge transfer during battery operation.

Electrochemical characterization further confirmed that the optimal vanadium doping level corresponds to a V/Mo atomic ratio of 0.161, which achieved the highest specific capacity of ~240 mA h g^{-1} along with excellent cycling stability. However, excessive doping levels (V/Mo > 0.161) led to capacity fading and increased structural degradation, reinforcing the existence of an optimal doping threshold beyond which electrochemical benefits diminish. The analysis of charge storage mechanisms through CV measurements at different scan rates revealed that vanadium doping favours a diffusion-controlled intercalation process, shifting the charge storage behaviour toward a more battery-like mechanism. This behaviour is advantageous for aluminium-ion batteries, as diffusion-controlled intercalation is associated with better cycling stability, higher reversibility, and improved long-term capacity retention. Moreover, *ex-situ* characterization of the cycled electrode confirmed that vanadium incorporation enhances the structural stability of h-MoO_3. SEM-EDS analysis of the V15 electrode (V/Mo atomic ratio = 0.161) revealed a homogeneous distribution of aluminium, suggesting effective chloroaluminate redox activity and uniform charge storage within the material. Furthermore, Raman spectroscopy confirmed that the h-MoO_3 structure remained intact after cycling, with no evidence of secondary phase formation, reinforcing its high stability in aluminium-ion batteries.

Comparison of these results with previously studied Ni-doped h-MoO_3, evidence that vanadium doping presents distinct advantages. While both strategies yield similar discharge capacities, vanadium-doped electrodes require a lower amount of binder and carbon black (70:20:10 vs. 55:25:20 for Ni-doped materials), indicating that vanadium incorporation improves intrinsic electronic conductivity. Additionally, vanadium-doped samples exhibit superior charge-discharge stability, with less fluctuation in capacity retention over extended cycles, making them more suitable for long-term applications. Overall, these findings confirm that vanadium doping is an effective strategy to optimize the electrochemical performance of h-MoO_3 for aluminium-ion batteries. By improving charge storage capacity, cycling stability, and electronic conductivity while maintaining structural integrity, vanadium-doped h-MoO_3 emerges as a promising cathode material for next-generation aluminium-ion batteries.

Acknowledgements

The authors would like to thank Imerys Graphite & Carbon and Fertiberia who kindly provided us with the carbon black and the urea used in this work. The authors are also indebted to the UCM XRD research assistance center and the CNME ELECMI - National Center for Electron Microscopy for scientific support. This work has been supported by UCM through project PR/23-30813. E.R.C. thanks to Spanish Ministry of Science and Innovation, project PID2021-126235OB-C32 funded by MCIN/ AEI/10.13039/501100011033/ and FEDER funds.

CRediT authorship contribution statement

Paloma Almodóvar: Conceptualization, Investigation, Data curation, Formal analysis, Writing – Original Draft. **Joaquín Calbet**: Investigation. **Inmaculada Álvarez-Serrano**: Investigation, Data curation, Writing – Review & Editing. **Enrique Rodríguez-Castellón**: Investigation, Data

curation. **María Luisa López**: Investigation, Data curation, Resources, Writing – Review & Editing, **Joaquín Chacón**: Supervision, Resources. **Carlos Díaz-Guerra**: Investigation, Data curation, Visualization, Validation, Writing – review & editing, Funding acquisition.

References

[1] G.A. Elia, K. V. Kravchyk, M. V. Kovalenko, J. Chacón, A. Holland, R.G.A. Wills, An overview and prospective on Al and Al-ion battery technologies, J. Power Sources. 481 (2021) 228870. https://doi.org/10.1016/j.jpowsour.2020.228870.

[2] J. Tu, W. Wang, H. Lei, M. Wang, C. Chang, S. Jiao, Design Strategies of High-Performance Positive Materials for Nonaqueous Rechargeable Aluminum Batteries: From Crystal Control to Battery Configuration. Small 18 (2022) 2201362. https://doi.org/10.1002/smll.202201362.

[3] J. Tu, W.-L. Song, H. Lei, Z. Yu, L.-L. Chen, M. Wang, S. Jiao, Nonaqueous Rechargeable Aluminum Batteries: Progresses, Challenges, and Perspectives, Chem. Rev. 121 (2021) 4903–4961. https://doi.org/10.3389/fchem.2019.00268.

[4] Y. Wang, J. Zhao, J. Lu, F. Yang, T. Wu, Towards sustainable energy storage of new low-cost aluminum batteries from fundamental study to industrial applications, J. Power Sources. 630 (2025) 236168. https://doi.org/10.1016/j.jpowsour.2025.236168.

[5] J. Zhao, Y. Chen, Z. An, M. Zhang, W. Wang, Q. Guo, Y. Li, S. Han, L. Zhang, Towards the next generation of sustainable aluminum-ion batteries: A review, Green Chem. 27 (2025) 352–378. https://doi.org/10.1039/d4gc04505j.

[6] P. Almodóvar, D.A. Giraldo, J. Chancón, I. Álvarez-Serrano, M.L. López, δ-MnO_2 Nanofibers: A Promising Cathode Material for New Aluminum-Ion Batteries, ChemElectroChem. 7 (2020) 2102–2106. https://doi.org/10.1002/celc.202000425.

[7] P. Almodóvar, N. Rey-Raap, S.L. Flores-López, B. Sotillo, L. Santos, M. Tinoco, J. Ramírez-Castellanos, I. Álvarez-Serrano, M.L. López, I. Cameán, A. Arenillas, J. Chacón, A.B. García, Enhancing Aluminium-Ion Battery Performance with Carbon Xerogel Cathodes, Batter. Supercaps. 7 (2024) e202400114. https://doi.org/10.1002/batt.202400114.

[8] H.J. Lunk, H. Hartl, M.A. Hartl, M.J.G. Fait, I.G. Shenderovich, M. Feist, T.A. Frisk, L.L. Daemen, D. Mauder, R. Eckelt, A.A. Gurinov, "Hexagonal molybdenum trioxide" - Known for 100 years and still a fount of new discoveries, Inorg. Chem. 49 (2010) 9400–9408. https://doi.org/10.1021/ic101103g.

[9] G. Zhu, M. Angell, C.J. Pan, M.C. Lin, H. Chen, C.J. Huang, J. Lin, A.J. Achazi, P. Kaghazchi, B.J. Hwang, H. Dai, Rechargeable aluminum batteries: effects of cations in ionic liquid electrolytes, RSC Adv. 9 (2019) 11322–11330. https://doi.org/10.1039/C9RA00765B.

[10] M. Malik, K.L. Ng, G. Azimi, Physicochemical characterization of $AlCl_3$-urea ionic liquid analogs: Speciation, conductivity, and electrochemical stability, Electrochim. Acta. 354 (2020) 136708. https://doi.org/10.1016/j.electacta.2020.136708.

[11] M. Angell, C.J. Pan, Y. Rong, C. Yuan, M.C. Lin, B.J. Hwang, H. Dai, High Coulombic efficiency aluminum-ion battery using an $AlCl_3$-urea ionic liquid analog electrolyte, Proc. Natl. Acad. Sci. U. S. A. 114 (2017) 834–839. https://doi.org/10.1073/pnas.1619795114.

[12] C. Wang, J. Li, H. Jiao, J. Tu, S. Jiao, The electrochemical behavior of an aluminum alloy anode for rechargeable Al-ion batteries using an $AlCl_3$-urea liquid electrolyte, RSC Adv. 7 (2017) 32288–32293. https://doi.org/10.1039/c7ra05860h.

[13] P. Almodóvar, D. Giraldo, C. Díaz-Guerra, J. Ramírez-Castellanos, J.M. González Calbet, J. Chacón, M.L. López, h-MoO_3/$AlCl_3$-Urea/Al: High performance and low-cost rechargeable Al-

ion battery, J. Power Sources. 516 (2021) 230656. https://doi.org/https://doi.org/10.1016/j.jpowsour.2021.230656.

[14] P. Almodóvar, I. Álvarez-Serrano, I. Llorente, M. L. López, J. Chacón, C. Díaz-Guerra, Nickel - Doped h - MoO_3 Cathodes : A High - Performance Material for Aluminum - Ion Batteries, Battery Energy (2025) e20240076. https://doi.org/10.1002/bte2.20240076.

[15] K. Lolupima, J. Cao, D. Zhang, C. Yang, X. Zhang, J. Qin, A review on the development of metals-doped Vanadium oxides for zinc-ion battery, J. Met. Mater. Miner. 34 (2024) 2084. https://doi.org/10.55713/jmmm.v34i3.2084.

[16] R.A.P. Camacho, R. Tian, J. Liu, S. Zhou, A. Wu, Electrochimica Acta Superior lithium-ion storage of V-doped MoO_3 nanosheets via plasma evaporation, Electrochim. Acta. 394 (2021) 139121. https://doi.org/10.1016/j.electacta.2021.139121.

[17] G. Qu, J. Wang, G. Liu, B. Tian, C. Su, Z. Chen, J.-P. Rueff, Z. Wang, Vanadium Doping Enhanced Electrochemical Performance of Molybdenum Oxide in Lithium-Ion Batteries, Adv. Funct. Mater. 29 (2019) 1805227. https://doi.org/https://doi.org/10.1002/adfm.201805227.

[18] G. Qu, C. Qiu, J. Wang, J. Tan, S. Jia, Z. Chen, J-P. Rueff, G. Zheng, C. Su, B. Tian, Phase engineering of Mo-V oxides for zinc-ion batteries, 65 (2022) 939–946. https://doi.org/10.21203/rs.3.rs-94180/v1

[19] K. Bhimani, A.S. Lakhnot, S. Sharma, M. Sharma, R.A. Panchal, V. Mahajani, N. Koratkar, Molybdenum Vanadium Oxides as Intercalation Hosts for Chloroaluminate Anions, Batteries 9 (2023) 92. https://doi.org/10.3390/batteries9020092.

[20] Y. Yan, W. Peng, B. Yuan, S. Li, J. Liang, Q. Han, S. Li, R. Hu, Hexagonal MoO_3 Anode with Extremely High Capacity and Cyclability for Lithium-Ion Battery: A Combined Theoretical and Experimental Study, ACS Applied Materials & Interfaces, 16(29) (2024) 37840-37852. https://doi.org/10.1021/acsami.4c03982.

[21] P. Almodóvar, M.L. López, J. Ramírez-Castellanos, S. Nappini, E. Magnano, J.M. González-Calbet, C. Díaz-Guerra, Synthesis, characterization and electrochemical assessment of hexagonal molybdenum trioxide (h-MoO_3) micro-composites with graphite, graphene and graphene oxide for lithium ion batteries, Electrochim. Acta. 365 (2021) 137355. https://doi.org/https://doi.org/10.1016/j.electacta.2020.137355.

[22] A. Chithambararaj, A.C. Bose, Investigation on structural, thermal, optical and sensing properties of meta-stable hexagonal MoO_3 nanocrystals of one dimensional structure, Beilstein J. Nanotechnol. 2 (2011) 585–592. https://doi.org/10.3762/bjnano.2.62.

[23] A. Ureña-Begara, Ferran Crunteanu, J.-P. Raskin, Raman and XPS characterization of vanadium oxide thin films with temperature, Appl. Surf. Sci. 403 (2017) 717–727. https://doi.org/10.1016/j.apsusc.2017.01.160.

[24] Y. Chen, K. Xie, Z.X. Liu, Determination of the position of V^{4+} as minor component in XPS spectra by difference spectra, Appl. Surf. Sci. 133 (1998) 221–224. https://doi.org/10.1016/S0169-4332(98)00202-5.

[25] O. Mougin, J. Dubois, A. Rousset, Metastable Hexagonal Vanadium Molybdate Study, J. Solid State Chem. 152 (2000) 353-360. https://doi.org/10.1006/jssc.2000.8663.

[26] P. Shvets, K. Maksimova, A. Goikhman, In situ XRD and Raman study of the phase transition in V_2O_5 xerogels, J. Non. Cryst. Solids. 625 (2024) 122751. https://doi.org/https://doi.org/10.1016/j.jnoncrysol.2023.122751.

[27] V. V Atuchin, T.A. Gavrilova, V.G. Kostrovsky, L.D. Pokrovsky, I.B. Troitskaia, Morphology and structure of hexagonal MoO_3 nanorods, Inorg. Mater. 44 (2008) 622. https://doi.org/10.1134/S0020168508060149.

[28] M.A. Bañares, I.E. Wachs, Molecular structures of supported metal oxide catalysts under different environments, J. Raman Spectrosc. 33 (2002) 359–380. https://doi.org/https://doi.org/10.1002/jrs.866.

[29] G.T. Went, L. Leu, A.T. Bell, Quantitative structural analysis of dispersed vanadia species in TiO_2(anatase)-supported V_2O_5, J. Catal. 134 (1992) 479–491. https://doi.org/https://doi.org/10.1016/0021-9517(92)90336-G.

[30] J.H. Xu, T. Schoetz, J.R. Mcmanus, V.R. Subramanian, W. Fields, R.J. Messinger, Tunable Pseudocapacitive Intercalation of Chloroaluminate Anions into Graphite Electrodes for Rechargeable Aluminum Batteries, J. Electrochem. Soc. 168 (2021) 60514. https://doi.org/10.1149/1945-7111/ac0648.

[31] J.M. Tarascon, M. Armand, Issues and challenges facing rechargeable lithium batteries, Nature. 414 (2001) 359–367. https://doi.org/10.1109/ICUWB.2008.4653360.